Heliyon 8 (2022) e10210

Contents lists available at ScienceDirect

Heliyon

journal homepage: www.cell.com/heliyon

Research article

A novel $CuBi_2O_4$/polyaniline composite as an efficient photocatalyst for ammonia degradation

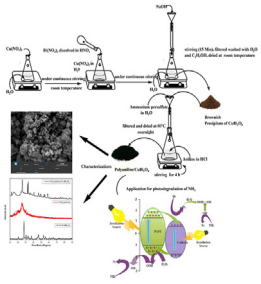
Nafees Ahmad [a,c], Jerry Anae [a], Mohammad Zain Khan [b], Suhail Sabir [b], Pablo Campo [a], Frederic Coulon [a,*]

[a] School of Water, Energy and Environment, Cranfield University, Cranfield, MK 43 0AL, UK
[b] Environmental Research Laboratory, Department of Chemistry, Aligarh Muslim University, Aligarh, India, 202002
[c] Department of Chemistry, Integral University, Lucknow, India, 226026

HIGHLIGHTS

- Novel $CuBi_2O_4$/PANI composite was synthesized via *in situ* polymerization of aniline.
- High surface area of $CuBi_2O_4$/PANI (45 m^2g^{-1}) exhibits higher efficiency towards adsorption and photocatalytic degradation of ammonia.
- Material shows synergistic effect by improving the redox ability for enhanced photodegradation of ammonia.
- Holes (h^+) and hydroxyl radicals (·OH) were confirmed as the prime reactive species for the photodegradation of NH_3.

GRAPHICAL ABSTRACT



ARTICLE INFO

Keywords:
Photocatalyst
In-situ polymerization
Kinetics
Scavengers
Electron-hole pairs

ABSTRACT

A novel polyaniline (PANI) coupled $CuBi_2O_4$ photocatalyst was successfully synthesized via in situ polymerization of aniline with pre-synthesized $CuBi_2O_4$ composites. The structure and morphology of the synthesized $CuBi_2O_4$/PANI composite photocatalyst were characterized by X-ray diffraction (XRD) and Fourier transform infrared spectroscopy (FTIR) and the photocatalytic performance were evaluated through degradation process of ammonia in water under visible light irradiation. The resultant $CuBi_2O_4$/PANI composite showed exceptional stability as its structure and morphology persisted even after being immersed in water for 2 days. The composite photocatalyst exhibited improved charge transport properties due to the electrical conductivity of the PANI protective layer, leading to enhanced photoelectrochemical activity in water and removal of ammonia. PANI with $CuBi_2O_4$ (10% wt) heterostructure was applied for photodegradation of ammonia and exhibited a 96% ammonia removal efficiency (30 mg/l with 0.1 g photocatalyst and 180 min), as compared to PANI (78%) and $CuBi_2O_4$ (70%). The degradation was attributed to the efficient charge transfer (e^- and h^+) and formation of reactive oxygen species upon simulated sunlight exposure. The present work suggests that the $CuBi_2O_4$/PANI photocatalyst can be synthesized in a simple process and provides an excellent adsorption capacity, high photocatalytic activity, long term stability, and reusability making it a promising alternative for ammonia removal from wastewater.

* Corresponding author.
E-mail address: f.coulon@cranfield.ac.uk (F. Coulon).

https://doi.org/10.1016/j.heliyon.2022.e10210
Received 18 March 2022; Received in revised form 27 May 2022; Accepted 3 August 2022
2405-8440/© 2022 The Author(s). Published by Elsevier Ltd. This is an open access article under the CC BY license (http://creativecommons.org/licenses/by/4.0/).

1. Introduction

Ammonia (NH_3 or NH_4^+) can have significant effect on both the environment and human health and negatively affect biodiversity. The main release source of ammonia in the environment is from agriculture activities such as man-made fertilizer application, fossil fuel, manure, and slurry management (Tang et al., 2021; Bao et al., 2022; Chai et al. 2021a, 2021b). High concentration of ammonia in water has detrimental effects leading to eutrophication or changes in species and reduces the efficiency of chlorine disinfectants in drinking water (Liu et al., 2017; Zhang et al., 2020).

Several treatment methods including air stripping (Ukwuani and Tao, 2016), ion exchange (Almutairi and Weatherley, 2015), adsorption (Qiang et al., 2020), biological nitrification-denitrification (Li et al., 2019) and breakpoint chlorination (Pressley et al., 1972) have been widely adopted for ammonia removal. These technologies, however, show drawbacks such as air stripping, which requires large amount of photocatalysts along with high energy consumption and further generate secondary air emissions to be treated (Ukwuani and Tao, 2016). Biological nitrification-denitrification is a relatively slow process that is susceptible to changes in temperature, dissolved oxygen, and pH (Ye et al., 2019). In physical process such as ion exchange, physical adsorption and air stripping, ammonia can only be transformed from the aqueous (NH_4^+-N) to vapour phase (NO_3^--N) rather than being converted to N_2 (Qiang et al., 2020). Hence the need of alternatives for removing NH_4^+-N from wastewater at lower energy and chemical costs.

Photocatalysis has been shown as a promising green technology that can degrade organic pollutants in water and reduce or oxidize inorganic pollutants (Ren et al., 2021). However, catalysts are often prone to self-etching during use. Studies have therefore focused on the construction of heterojunction structures and doping to improve performance and to restore photocatalytic performance by oxidative reduction of deactivated photocatalysts. In this regard, a few semiconductor nanoparticles and nanocomposites such as g-C_3N_4, SiO_2-BiOCl and reduced graphene oxide encapsulated into polymer matrices such Polyaniline (PANI), polypyrrole, polythiophene and polyfuran have been used (Sethuraman et al., 2021; Tian et al., 2017; Zheng et al., 2021; Yan et al., 2022; Ahmad et al. 2017, 2019). Among the polymer matrices, PANI has shown excellent photocatalytic performance because of its redox properties, tuneable bandgap energy with suitable configuration of conduction band (CB)-valence band (VB), higher surface area, and better cost-effectiveness than nanoparticles (Xiong et al., 2022; Tanwar et al., 2017; Xu et al., 2017). Conversely, recombination of photo-induced electron-hole pairs can only happen when PANI is irradiated during photocatalysis, which limits the efficacy of the process and removal of organic contaminants (Kundu et al., 2017; Belabed et al., 2021). To overcome the issue of recombination of photo-induced electron-hole, heterojunction between PANI and the semiconductor is often recommended.

Until now, the use and application of polymer nanocomposites for the photocatalytic degradation of ammonia is limited. In this study, a novel $CuBi_2O_4$/PANI composite with photocatalytic activity is synthesized for the degradation of ammonia under the influence of light emitted diode (LED) irradiation. A series of photocatalysts were synthesized by in-situ polymerization of aniline and $CuBi_2O_4$ with a low temperature method to assess their performance for the removal of ammonia in water. A 15 W LED has been used as the irradiation source which consume less power supply than other UV and visible light sources. The factors affecting the adsorption capacity and photodegradation efficiency such as ammonia load, catalyst concentration, and the radiation time, as well as the PANI and $CuBi_2O_4$ content were investigated for process optimisation and mitigation strategies.

2. Materials and method

2.1. Chemicals and reagents

All the chemicals used in the study were of analytical grade. Ammonium persulfate ($(NH_4)_2S_2O_8$), aniline C6H5NH2, hydrochloric Acid (HCl) (37%), copper nitrate tri hydrate (CuNO3.3H2O), bismuth nitrate penta hydrate ($BiNO_3.5H_2O$), sodium hydroxide (NaOH), nitric Acid (HNO_3) (98%), ammonia (NH_3), Nessler's Reagent (K_2HgI_4) (alkaline solution of mercuric (II) iodide and potassium iodide) were procured from Sigma Aldrich (USA).

3. Experimental section

3.1. Synthesis of the $CuBi_2O_4$

Synthesis of $CuBi_2O_4$ was carried out in accordance to Wang et al. (2015). Briefly, a solution of $Cu(NO_3)_2 \bullet 3H_2O$ (1.5 mmol) in water was mixed with 3 mmol of $Bi(NO_3)_3 \bullet 5H_2O$, which was prepared beforehand in a nitric acid solution (0.1 M), under continuous stirring for 15 min at room temperature. Then10 ml of NaOH (6 M) was added to the solution and stirred for 30 min at room temperature. The crystals were then separated by filtration and sequentially washed three times with 10 ml of deionised water followed by ethanol. The filtrate was oven dried overnight at 60 °C. The synthesis was done twice before performing the characterisation analyses and the photocatalytic experiments.

3.2. Synthesis of PANI and $CuBi_2O_4$/PANI via oxidative polymerization method

PANI was synthesized by chemical oxidative polymerization of the aniline monomer with ammonium persulphate (Ahmad et al., 2019a,b). A 1:1 solution of aniline (25 ml, 0.1 M prepared in 1 M HCl) and ammonium persulfate (25 ml, 0.1 M prepared in distilled water) were used for synthesis. Ammonium persulfate was added dropwise to the aniline solution and stirred for 4 h. A dark green precipitate was obtained and separated with a 150 mm filter paper (Whatman pore size 11 μm). The precipitate was then washed with 10 ml of distilled water followed by 10 mL of acetone and dried overnight at 60 °C. The PANI/$CuBi_2O_4$ composite was prepared with the same method in which pre-synthesized $CuBi_2O_4$ (1:3 (monomer to $CuBi_2O_4$) was added and sonicated for 15 min. The ratio of $CuBi_2O_4$ to aniline monomer was 1:3. An overview of the steps for the synthesis of PANI/$CuBi_2O_4$ composite is shown in Figure 1.

3.3. Composite materials characterisation

The crystal structure and purity of PANI, $CuBi_2O_4$ and $CuBi_2O_4$/PANI were established with a Siemens D5005 X-ray diffractometer (XRD). Surface morphology and elemental composition of the materials were obtained by scanning electron microscopy (SEM) coupled with energy dispersive X-ray spectroscopy (Tescan VEGA 3); size and shape of the particles were determined by transmission electron microscopy (TEM) (JEM 1400, JEOL, Japan). A PerkinElmer ultraviolet-diffuse reflectance Win Lab spectrometer (UV-DRS) was used to obtain the bandgap energy of the photocatalysts. The recombination of charge carriers during the photodegradation was evaluated from the fluorescence spectra (Horiba Scientific, Spectrofluorometer). The elemental states of the photocatalysts were determined by X-ray photon spectroscopy (XPS) (Kratos Axis Supra- X ray source (Mono Al kα) and energy -1486.7 eV) and the surface area, pore size and pore volumes were calculated by Brunauer–Emmett–Teller (Quantachrome NOVA 4000e). Ammonia

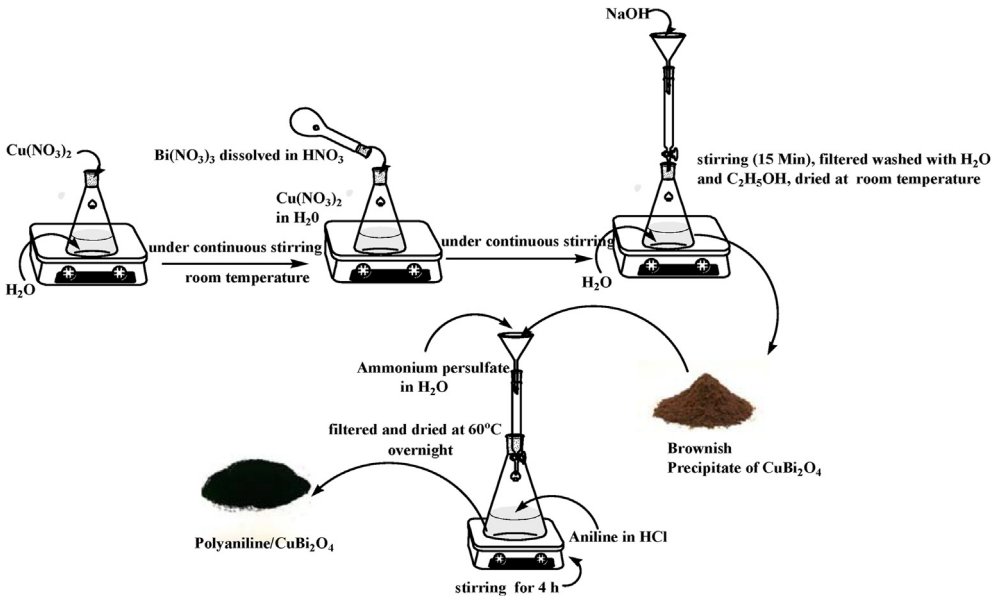


Figure 1. Overview of the steps for the synthesis of $CuBi_2O_4$/PANI composite.

concentrations were measured with an UV–VIS spectrophotometer (Jenway 6715, UK) with the Nessler's reagent as reported by Liu et al. (2018).

3.4. Photocatalytic activity and recyclability

The photocatalytic activity was evaluated by examining the photodegradation of ammonia in a 100 ml photoreactor equipped with visible light irradiation lamp (15 W LED). A mixture of 0.1 g of photocatalyst and 100 ml of the ammonia solution in the reactor was stirred continuously for 3 h with a magnetic bar till the end of the experiment. An air pump (Victsing aquarium air pump) with constant air flow was also used to supply atmospheric oxygen. Prior to LED irradiation, the solution was stirred for 20 min in the dark to attain equilibrium between the ammonia and the photocatalyst. Thereafter, the whole mixture was irradiated, and 5-ml aliquots were collected every 30 min to measure ammonia's concentration. Ammonia concentration was determined using the Nessler's reagent. Photodegraded sample of ammonia was determined by UV-visible spectrophotometer at maximum wavelength of 382 nm. A blank experiment was also carried out in which no photocatalyst was added. All conditions were carried out in triplicate. The absorbance was recorded between 300-600 nm. The degradation efficiency was calculated with Eq. (1):

$$\text{Degradation efficiency } (\%) = \frac{C_0 - C_t}{C_0} \times 100 \quad (1)$$

where C_0 is the initial concentration of the ammonia at equilibrium and C_t is the concentration at a given time t.

The stability and durability of the photocatalyst PANI coupled with $CuBi_2O_4$ were also investigated. Hence after each ammonia degradation experiment, the photocatalyst was recovered, washed with distilled water and acetone to remove any impurities, and dried overnight at room temperature. The photocatalyst was used in five consecutive cycles to check the durability.

To study the effect of the pH on the photodegradation of ammonia, the photocatalytic experiments were carried out at pH 5, 7, 9, 11 and 13. The pH was adjusted with 0.1 M solutions of either NaOH or HCl before the addition of the photocatalysts; each pH condition was tested in duplicate.

3.5. Degradation mechanisms

To identify the main reactive species responsible for the photodegradation of ammonia, *t*-butyl alcohol (TBA) and disodium ethylenediaminetetraacetic acid (EDTA) scavengers were used as quenching agents for •OH and h^+, respectively. Both TBA (0.5 ml) and EDTA (0.025 g) were added to 100 ml of aqueous solution of ammonia used in separate experiments to quench •OH and h^+ respectively. The experimental conditions were then the same as described in subsection 2.4.

4. Result and discussion

4.1. Purity and structure analysis

The crystal structure and phase purity of $CuBi_2O_4$, PANI and $CuBi_2O_4$/PANI were confirmed by XRD (Figure 2). Diffraction peaks at 2θ of 20.7°, 27.83°, 29.45°, 30.74°, 33.22°, 34.24°, 37.44°, 44.71°, 46.63°, 47.91°, 53.03°, 55.48°, 60.60° and 65.98° with corresponding *hkl* values (2,0,0), (2,1,1), (2,2,0), (0,0,2), (3,1,0), (1,1,2), (2,0,2), (3,3,0), (4,1,1), (4,2,0), (2,1,3), (3,3,2), (5,2,1) and (4,1,3) show the tetragonal geometry of $CuBi_2O_4$ particles (JCPDS card of $CuBi_2O_4$ (42-0334) (Sharma et al.,

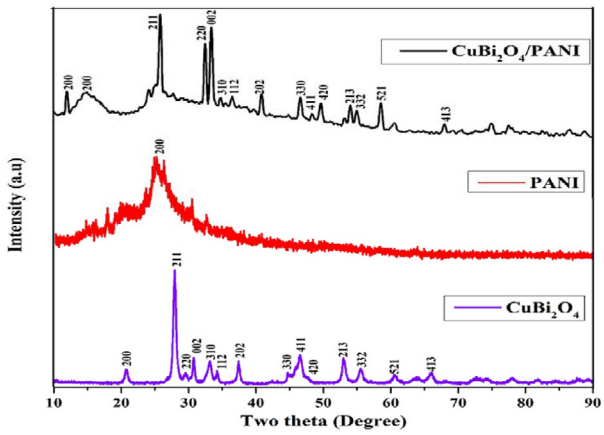


Figure 2. XRD spectra of the as synthesized materials $CuBi_2O_4$, PANI and $CuBi_2O_4$/PANI.

2016; Wang et al., 2018). The characteristic hump at 2θ of 25.32° with corresponding *hkl* value of (2,0,0) confirmed the presence of PANI (Mitra et al., 2019). However, in the case of $CuBi_2O_4$/PANI, a clear shift in the peaks toward the lower and higher theta values highlight a mismatch of ionic radii and angle of strain in the composite which confirms the formation of composites (Goransson et al., 2019; Ahmad et al., 2019; Alam et al., 2018). The peak shifts also indicate that the bond formation between PANI and $CuBi_2O_4$ is occurring which was further confirmed with the XPS analysis.

The crystallite size of the particles was calculated with the Scherrer's formula (Equation 2) as follows:

$$d = 0.9\lambda/\beta\cos\theta \quad (2)$$

where d is the size of the crystallite, λ is the x-ray wavelength, β is the full width at half maxima and θ is the diffraction angle between 10 and 80°. The crystallite size ranged between 18.9, 25.4, and 28.9 nm for $CuBi_2O_4$, PANI and $CuBi_2O_4$/PANI composite, respectively. The presence of the sharp diffraction peaks in $CuBi_2O_4$/PANI and $CuBi_2O_4$ confirmed the crystalline nature of the photocatalyst and the formation of $CuBi_2O_4$/PANI composite.

4.2. Morphological characterisation and elemental composition analysis

Surface morphology and shape of $CuBi_2O_4$, PANI and $CuBi_2O_4$/PANI are shown in Figure 3. The hedgehog-like microspheres agglomerated in packed nanorods are the $CuBi_2O_4$ particles (Figure 3, panels a and b). The porous surface of PANI is shown in Figure 3c. The porosity of the surface helps the interaction between ammonia and the photocatalyst. The PANI/$CuBi_2O_4$ composite shape is shown in Figure 3d. The attached microspheres of $CuBi_2O_4$ particles on the surface of the PANI can easily be observed, which implies that the chemical interaction of the PANI and $CuBi_2O_4$ particles was achieved effectively.

EDX image and elemental mapping of the PANI/$CuBi_2O_4$ composite confirmed the presence and distribution of constituent elements (Cu, Bi, O, N and C) and the as shown in Fig.S1 (Supporting Information).

TEM images of the photocatalysts are presented in Figure 4; rod shaped $CuBi_2O_4$ can be seen in Figure 4 panels and b. Panels d and e in Figure 4 show the surface of the PANI and the contact between the PANI and $CuBi_2O_4$. TEM images of the $CuBi_2O_4$ nanorods can also be correlated to the SEM images showing the agglomerated nanorods of the $CuBi_2O_4$ particles (Wang et al., 2015). The averaged particles size of the PANI, $CuBi_2O_4$ and $CuBi_2O_4$/PANI was 29.03 ± 1.2 nm, 21 ± 1.0 nm and 15.76 ± 1.5 nm, respectively.

4.3. Chemical state of $CuBi_2O_4$ and PANI/$CuBi_2O_4$ photocatalysts

The XPS analysis was performed to characterise the chemical charge states, the surface elemental composition of the $CuBi_2O_4$ and $CuBi_2O_4$/PANI photocatalysts and to identify possible impurities (Figure 5). The photoelectron peaks of Cu, Bi, O, C, and N elements were clearly identified. The binding energies of the elements are shown in Table 1.

In pure $CuBi_2O_4$, the binding energy peaks of (Cu $2p_{3/2}$) and (Cu $2p_{1/2}$) are located at 929.24 and 949.44 eV; (Bi $4f_{7/2}$) and (Bi $4f_{5/2}$) peaks are located at 158.93 and 164.23 eV while (O 1s), owing to lattice oxygen of $CuBi_2O_4$, is located at 527.63 eV. These peaks are slightly shifted in PANI/$CuBi_2O_4$ which confirmed the heterojunction between PANI and $CuBi_2O_4$. Our measured values are in good agreement with those reported by Shi et al. (2017) who reported 934 and 954 eV for Cu $2p_{3/2}$ and Cu $2p_{1/2}$, respectively and 158.5 and 164 eV for (Bi $4f_{7/2}$) and (Bi $4f_{5/2}$). For PANI-$CuBi_2O_4$, the binding energy peaks (Cu $2p_{3/2}$ -932.3 eV), Cu $2p_{1/2}$-948.4 eV), (Bi $4f_{7/2}$- 154.9 eV), (Bi $4f_{5/2}$- 166.4 eV), (O 1s- 525.51 eV) (C 1s-284.19 eV) and (N 1s-399.1 eV) were identified which indicates the chemical interaction between PANI and $CuBi_2O_4$ (Bano et al., 2018). The C 1s spectrum at 284.19 eV confirmed the sp^2 hybridised carbon and the N 1s spectrum at 399.1 eV confirmed the N-H bond in the PANI (Guo et al., 2017).

4.4. BET analysis

The specific surface areas of the catalysts were estimated by the Brunauer–Emmett–Teller (BET) method from the nitrogen adsorption-

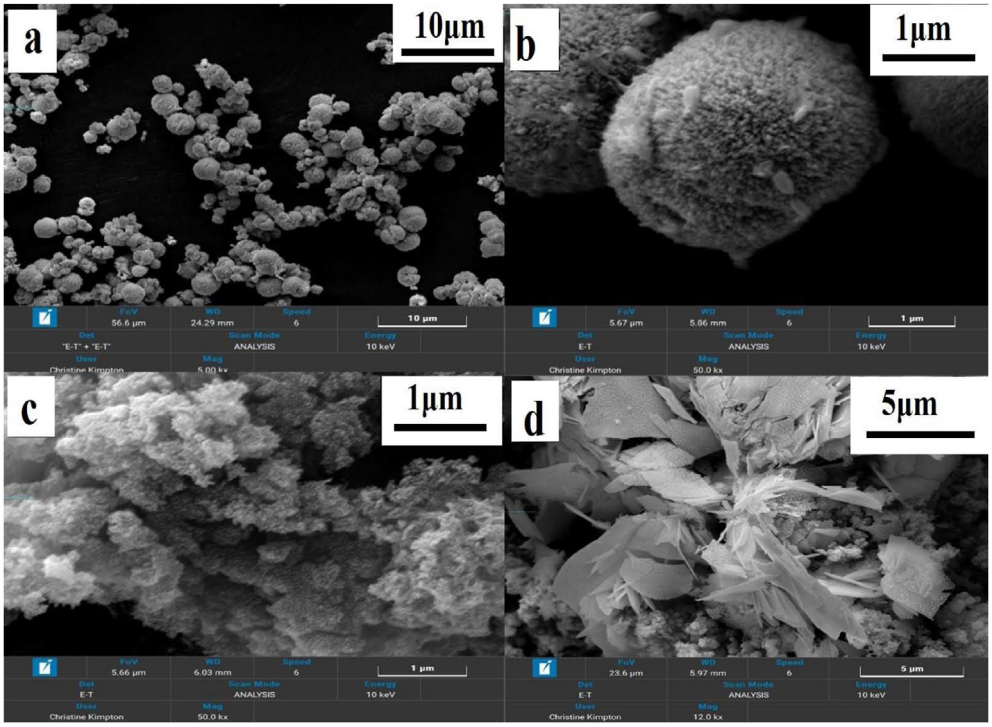


Figure 3. SEM images of as synthesized materials $CuBi_2O_4$ (a, b), PANI (c) and $CuBi_2O_4$/PANI (d).

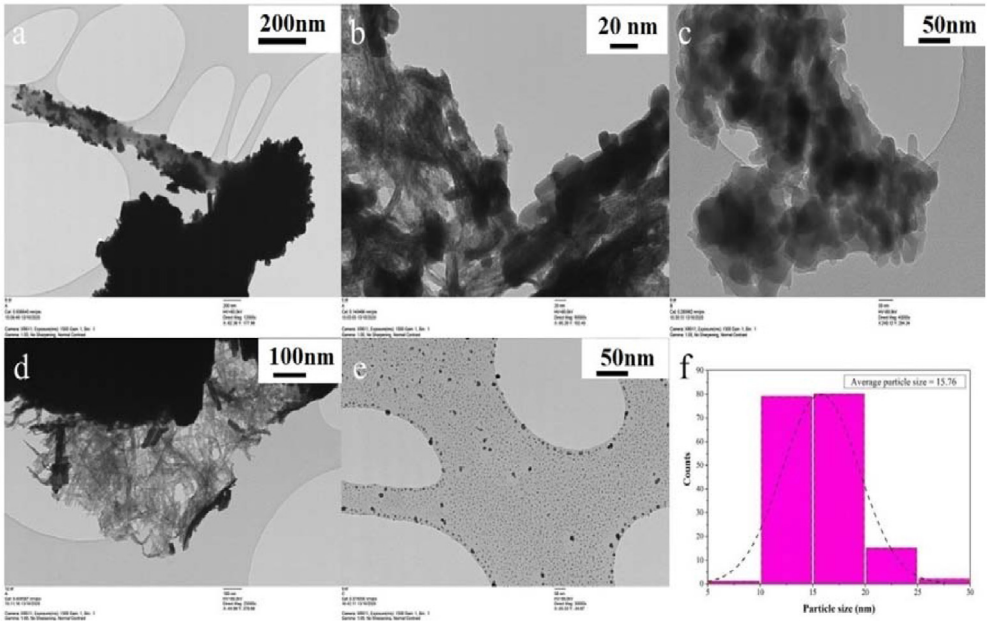


Figure 4. TEM image of $CuBi_2O_4$ (a, b), PANI (c) and $CuBi_2O_4$/PANI (d, e) and particle size distribution (f).

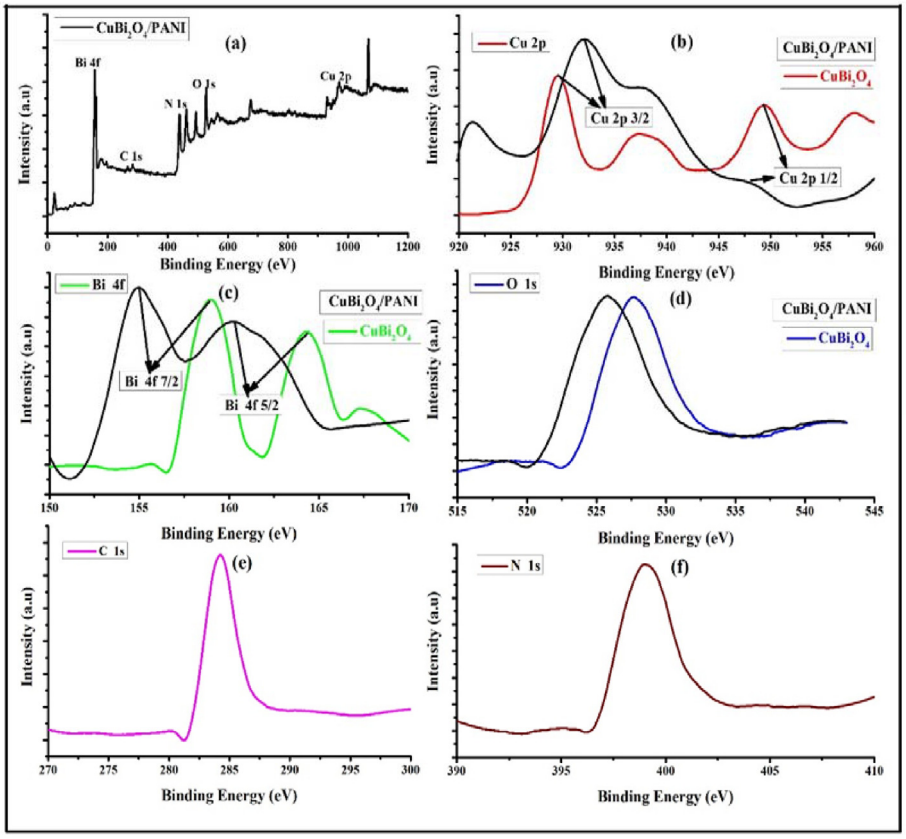


Figure 5. X ray photon survey spectra of (a) $CuBi_2O_4$/PANI composites (b) Cu 2p (c) Bi 4f (d) O 1s (e) C 1s and (f) N 1s recorded at room temperature.

desorption isotherm. The BET isotherms pore volumes and pore surface areas are shown in Figure 6a. Surface areas, pore diameters and pore volumes of the photocatalysts are summarised in Table 2. $CuBi_2O_4$/PANI exhibits higher surface area than either pure PANI or $CuBi_2O_4$; this was due to the doping of $CuBi_2O_4$ into the polymer. The surface area increases as particle size decreases. The higher surface area of $CuBi_2O_4$/PANI is due to the porous surface of polyaniline in which $CuBi_2O_4$ particles are settled down therefore reduces the size of PANI/$CuBi_2O_4$ (Dubois et al., 2011).

4.5. Bandgap energy analysis and calculation of edge band potential

To elucidate the photocatalytic mechanism, bandgap energy and edge band potential of the conduction band and valence band were investi-

Table: 1. Representative elements with corresponding binding energies.

Elemental states	Binding Energy (eV)
(Cu $2p_{3/2}$)	929.24
(Cu $2p_{1/2}$)	949.44
(Bi $4f_{7/2}$)	158.93
(Bi $4f_{5/2}$)	164.23
(O 1s)	527.63
(C 1s)	284.19
(N 1s)	399.1

gated by the Tauc plot (Figure 7) based on the Kubelka Munk Function formula (Equation 3):

$$(hv.\alpha) = (Ahv - Eg)^{n/2} \quad (3)$$

where α is proportional to F(R), which is Kubelka Munk function, ν is the frequency, A is the proportionality constant and Eg is the bandgap energy. Now it can be written as shown in Eq. (4),

$$\{(hv.F(R)\} = (Ahv - Eg)^{n/2} \quad (4)$$

The value of n is determined by n = 1 or 4 for direct and indirect allowed transition, respectively. The indirect transition (n = 4) has been considered to calculate the bandgap of PANI and $CuBi_2O_4$.

As shown in Figure 7, the respective bandgap energies for $CuBi_2O_4$ and $CuBi_2O_4$/PANI were 1.5 and 1.7 eV (Arai et al., 2007). The bandgap energy of the pure PANI was 2.1 eV as previously calculated by Ahmad et al. (2019a,b).

With the help of these bandgap energy values, conduction band (CB) and valence band (VB) potentials of the photocatalysts were calculate with Eqs. (5) and (6):

$$E_{VB} = X - E^c + 0.5E_g \quad (5)$$

$$E_{CB} = E_{VB} - E_g \quad (6)$$

where E_{VB} and E_{CB} are the VB and CB edge potential of the photocatalyst, E^c is the energy of free electrons on hydrogen's scale (i.e. 4.5 eV) and X is the geometric mean of the electronegativity of the constituent atoms of the photocatalyst. The respective conduction band potentials for PANI and $CuBi_2O_4$ were -1.38 and -0.61eV vs normal hydrogen electrode (NHE); the valence band potential of the PANI and $CuBi_2O_4$ were 0.8 and 1.13 eV, respectively.

4.6. Photocatalytic activity and extent of ammonia degradation

The photodegradation activity of the photocatalysts was checked by degrading ammonia in water. The rate constants of the photocatalytic reaction were fitted to zero-order kinetics. Table 3 list constant rates and removal extents (Table 3). The plots of Ln C vs time and Concentration vs time are shown in Figures S2 and S3 (Supporting information).

The photocatalytic experiments for the degradation of ammonia was repeated three times to ensure the applicability of the photocatalyst. The kinetics of ammonia photodegradation along the UV-visible spectra of the photodegraded ammonia in water samples and the rate constant of photocatalysts are shown in Figure 8.

Photocatalytic process started with the irradiation of LED lights. Upon irradiation, PANI was excited and generates electron-hole pairs in the highest occupied molecular orbital (HOMO) and the lowest unoccupied molecular orbital (LUMO), respectively. When $CuBi_2O_4$ was irradiated with LED, it absorbed the photons and got excited and then the electrons travelled to the conduction band (CB) leaving holes in the valence band (VB) as shown in Figure 9.

The electrons in the CB of the $CuBi_2O_4$ were in an unstable state and tended to occupy stable state, thus recombining with the holes. In this case, there were fewer electrons available to form ROS through redox reaction. Hence, the ammonia degradation by photocatalytic activity was

Table: 2. Surface area, pore diameter and pore volume of photocatalyst.

Catalyst	BET surface area, (m^2g^{-1})	BJH Pore diameter (nm)	Total BJH Pore volume, (cm^3g^{-1})
$CuBi_2O_4$	16.46	3.84	0.045
PANI	42.28	1.54	0.20
$CuBi_2O_4$/PANI	45.51	1.50	0.19

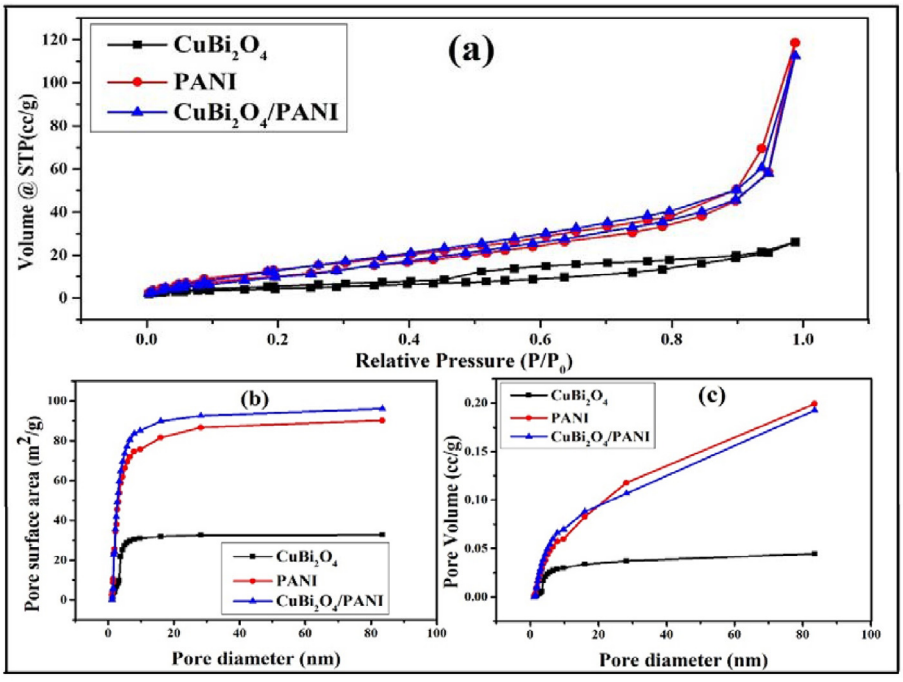


Figure 6. (a) BET isotherm, (b) pore surface area and (c) pore volume.

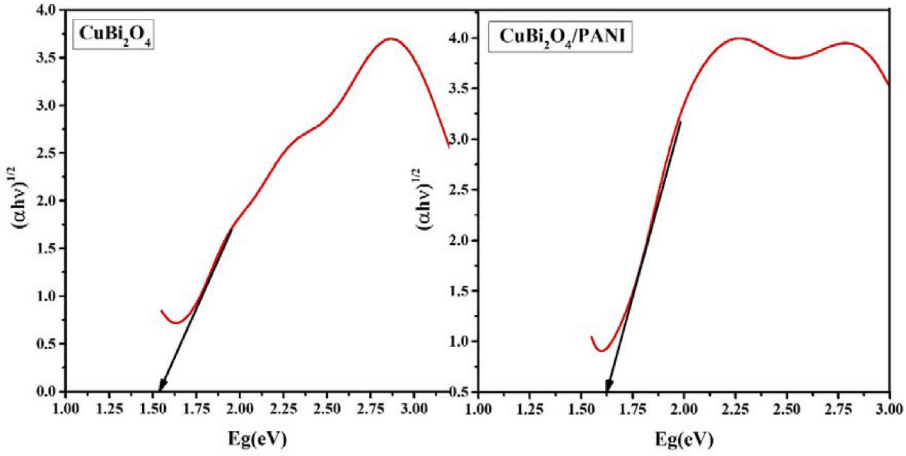


Figure 7. Tauc plot of $CuBi_2O_4$ and $CuBi_2O_4$/PANI composites.

Table: 3. Table representing the rate constants and degradation efficiencies of the photocatalyst.

Photocatalysts	Rate constants (min^{-1})	Degradation efficiency (%)
$CuBi_2O_4$	0.6475×10^{-2}	70
PANI	0.8896×10^{-2}	78
$CuBi_2O_4$/PANI	1.28×10^{-2}	96

quite slow; similarly, the PANI photodegradation efficiency was only of 78% for ammonia removal and this was due to higher recombination rates of electron and holes. In contrast, the combined $CuBi_2O_4$/PANI catalyst had the highest photocatalytic activity achieving over 96% removal of ammonia within 180 min. The formation of composites of $CuBi_2O_4$ with PANI reduced the recombination of electrons and holes and contributed to the formation of hydroxyl radical. The higher edge band potential of the PANI (−1.38 eV) compared to $CuBi_2O_4$ (−0.61 eV)

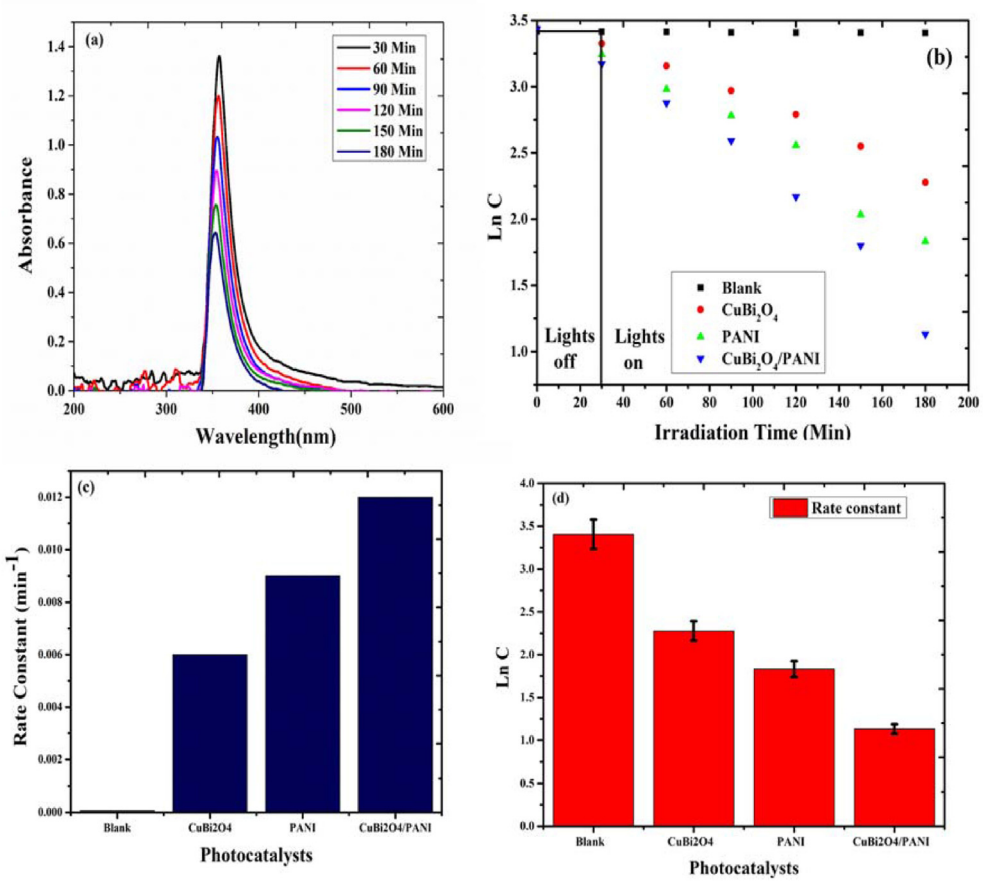


Figure 8. (a) UV-visible spectra of the photodegraded ammonia in water samples (b) Kinetics of photodegradation(c) rate constant of various photocatalyst against ammonia and (d) Standard deviation value of the kinetics of photodegradation from three independent replicates.

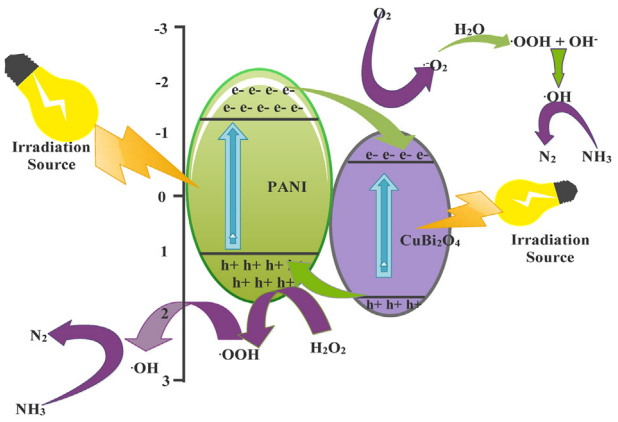


Figure 9. Proposed photocatalytic mechanism for the degradation of ammonia.

allowed the electrons of the LUMO of PANI to flow easily toward the $CuBi_2O_4$ particles scattered on the surface of PANI. In this way, the LUMO excited electrons of PANI, which are supposed to acquire a stable state, were combined with the excited electrons of the $CuBi_2O_4$ and thus suppress the recombination of electron-hole pairs of the PANI. As a result of the surface plasmon resonance (SPR) effect together with the electrons transferred from PANI, the photo excited electrons of $CuBi_2O_4$ convert the molecular tosuperoxide $\dot{O}_2$. These $\dot{O}_2$ molecules will then react with H_2O molecules to form $^{\bullet}OOH$ and OH^- and subsequently form H_2O_2. The generated holes in the HOMO of PANI then reacted with the H_2O_2 molecule and produced $\dot{O}H$ radicals. The ROS generated during the redox process (h^+ and $\dot{O}H$) contributed to the conversion of ammonia into nitrogen. The following reactions (7-16) describe the mechanism of photodegradation:

$$PANI + CuBi_2O_4 + hu \rightarrow PANI/CuBi_2O_4\ (h^+,\ e^-) \quad (7)$$

$$PANI\ (e^-) + O_2 \rightarrow \cdot O_2^- \quad (8)$$

$$H_2O + \cdot O_{2-} \rightarrow \cdot OOH + OH^- \quad (9)$$

$$\cdot OOH + H_2O \rightarrow \cdot OH + H_2O_2 \quad (10)$$

$$H_2O_2 + h^+ \rightarrow \cdot OOH + H^+ \quad (11)$$

$$H_2O_2 + \cdot OOH \rightarrow \cdot OH + H_2O + O_2 \quad (12)$$

The · OH generated react with ammonia to produce nitrogen

$$NH_3 + \cdot OH \rightarrow NH_2 + H_2O \quad (13)$$

$$NH_2 + \cdot OH \rightarrow NH + H_2O \quad (14)$$

$$NH + \cdot OH \rightarrow N + H_2O \quad (15)$$

$$NH_3 + h^+ \rightarrow N_2 + H^+ \quad (16)$$

In the mechanistic approach for the degradation of ammonia, $CuBi_2O_4$ particles facilitate the efficient separation of charge carriers, which increases lifetime and enhances degradation efficiency. The photocatalytic activity of the novel $CuBi_2O_4$/PANI composite is high compared to those reported in literature for ammonia (Table 4).

4.7. Effect of pH on degradation of ammonia and photoluminescence studies

Photodegradation efficiency is significantly influenced by pH (Shavisi et al., 2014; Altomare et al., 2012). The optimum pH was 11 for the degradation of ammonia in water. At basic pH, the formation of hydroxide ion and subsequently into hydroxyl radical favours the photodegradation of ammonia as shown in Figure 10a. Degradation efficiency increased from 55 to 90% up to pH 11 and decreased to 75% at pH 13. This was due to the competitive adsorption of hydroxyl radical on the surface of the photocatalyst which lowers the degradation efficiency.

Further, to check the recombination behaviour of the photogenerated electron and hole pairs, fluorescence spectroscopy was used. The recombination rate of electrons and holes are directly proportional to photocatalytic activity (Bano et al., 2019; Shafi et al., 2019). Figure 10b shows photoluminescence (PL) intensity of $CuBi_2O_4$, PANI and $CuBi_2O_4$/PANI. Higher PL intensities for PANI and $CuBi_2O_4$ indicate higher recombination rates of photogenerated electrons and holes, which translates to a lower photocatalytic activity. Conversely, the lower PL intensity observed for $CuBi_2O_4$/PANI was due to a lower recombination of electrons and holes that led to higher photocatalytic activity.

4.8. Tracking of the reactive species and durability of photocatalyst

IPA and EDTA were introduced to the photocatalytic degradation of ammonia with $CuBi_2O_4$/PANI to observe the effect $^{\bullet}OH$ and h^+ respectively. The rate constant of $CuBi_2O_4$/PANI declined when the scavengers were added (Fig. 11a and b). Both holes and hydroxyl radicals can contribute to ammonia degradation. Nevertheless, holes are the primary reactive species involved in such process, as holes produce hydroxyl radicals by oxidation of water molecules.

To assess the durability of $CuBi_2O_4$/PANI, the same photocatalyst was used for five consecutive times. Hence, the photocatalyst was recovered after each experiment, washed with distilled water and acetone, and dried for 12 h at 60 °C. As Figure 11c shows, the photocatalytic efficiency decreased by less than 2% after each experiment. Overall, the efficiency

Table: 4. Comparison of photodegradation efficiency of several photocatalysts for ammonia removal.

S.No	Photocatalyst	Ammonia (mg/l)	Photocatalyst (g)	Removal Efficiency (%)	Irradiation time (min)	Irradiation source	Reference
1	Ag_3PO_4-CaO	340	1.25	70	240	Visible lamp 53 mW/cm^2	Shavisi and Sharifnia, 2018
2	Zinc Ferrite/Activated Carbon	100	1.5	90	180	High pressure mercury lamp 300 W	Ye et al., (2019)
3	Cu/ZnO/rGO	50	0.2	83	120	High pressure mercury lamp 125 W	He et al., (2018)
4	TiO_2-ZnO/LECA	400	25	95	180	High pressure mercury lamp 125 W	Mohammadi et al., (2016)
5	UiO-66(Ti)-Fe_3O_4-WO_3	30	0.125	92	60	LEDs (14.4 W/m, 12 v)	Bahmani et al., (2020)
6	TiO_2 -Perlite	170	11.7	68	180	125 W Hg lamp	Shavisi et al., (2014)
7	α-MnO_2/N-Doped Graphene	100	0.1	93	480	NIR light irradiation	Liu et al., (2018)
8	Biochar carbon-doped TiO_2/CuO	100	0.03	99	120	25 W UV lamp	Peng et al., (2019)
9	TiO_2/LECA	975	125	96	4320	Solar Light	Shavisi et al., (2014)
10	PANI-$CuBi_2O_4$	30	0.1	96	180	LEDs (15 W)	Present study

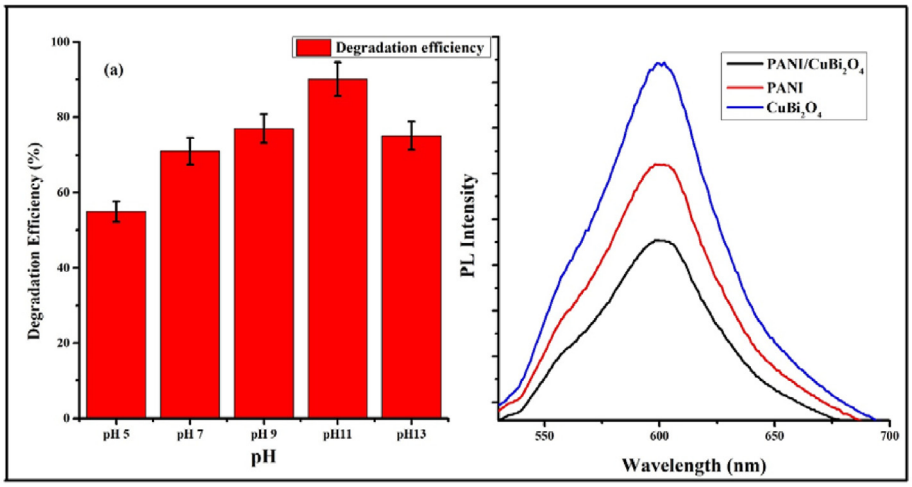


Figure 10. Effect of pH on the photodegradation of ammonia (a) and PL spectra of the photocatalyst to check the recombination behaviour of electron and holes (b).

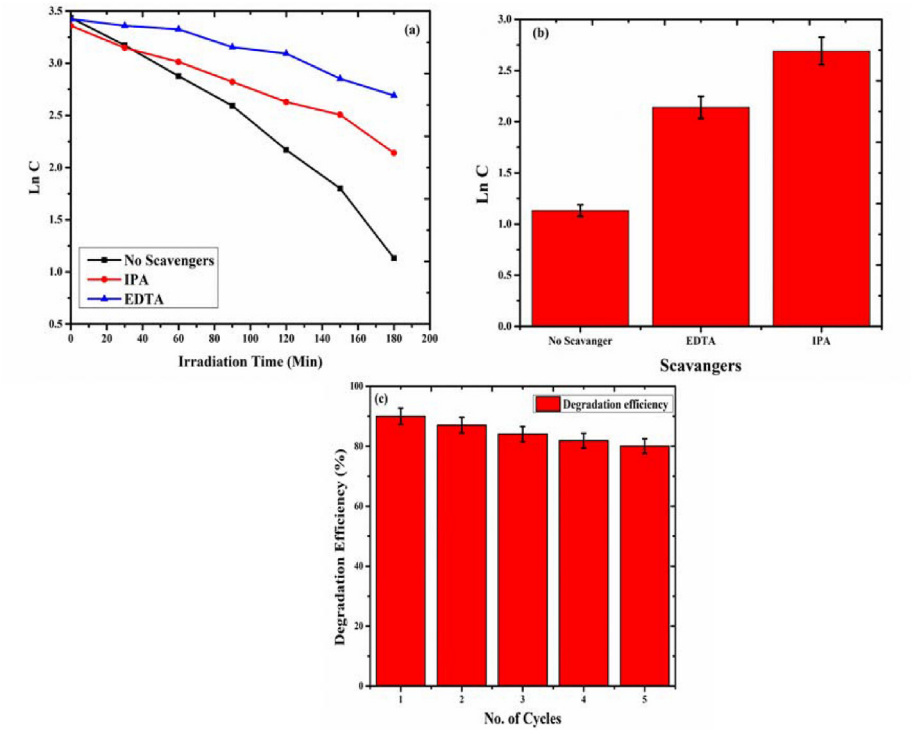


Figure 11. (a) Trapping experiments by holes and hydroxyl radicals (b) standard deviation of the trapping experiment and (c) recycling experiment of $CuBi_2O_4$/PANI photocatalyst.

was found to be <10% lower after the five consecutive tests. The decreased in the percentage removal was attributed to loss of photocatalyst particles after each use.

5. Conclusions

While PANI and $CuBi_2O_4$ showed good performance, the $CuBi_2O_4$/PANI composite provided better activity towards the photodegradation of ammonia in water. The removal extent for $CuBi_2O_4$/PANI was 96% whereas the respective values for $CuBi_2O_4$ and PANI were 70% and 78%. $CuBi_2O_4$/PANI outperformed the other materials owing to a higher electron and holes separation, lower recombination rates of electron and holes, and greater surface area. Both holes and hydroxyl radicals were accountable for the degradation of ammonia, but holes were the primary reactive species. $CuBi_2O_4$/PANI also exhibited reusability properties without compromising its activity. Based on the results and generation of reactive species responsible, it can be concluded that $CuBi_2O_4$/PANI is a promising photocatalyst for the treatment ammonia affluent.

Declarations

Author contribution statement

Nafees Ahmad: Conceived and designed the experiments; Performed the experiments; Analyzed and interpreted the data; Wrote the paper.

Jerry Anae: Contributed reagents, materials, analysis tools or data; Wrote the paper.

Mohammad Zain Khan, Suhail Sabir, Pablo Campo & Frederic Coulon: Conceived and designed the experiments; Wrote the paper.

Funding statement

Nafees Ahmad was supported by Commonwealth Foundation [INCN-2019-35].

Data availability statement

Data included in article/supp. material/referenced in article.

Declaration of interests statement

The corresponding author Prof Frederic Coulon is one of the Section Editor of the Environment Section.

Additional information

Supplementary content related to this article has been published online at https://doi.org/10.1016/j.heliyon.2022.e10210.

Unlisted reference

Shaveisi et al. 2018

Acknowledgements

Authors are thankful to the School of Water, Environment and Energy for providing necessary instrumentation facilities.

References

Ahmad, N., Sultana, S., Azam, A., Sabir, S., Khan, M.Z., 2017. Novel bio-nanocomposite materials for enhanced biodegradability and photocatalytic activity. New J. Chem. 41 (18), 10198–10207.

Ahmad, N., Sultana, S., Faisal, S.M., Ahmed, A., Sabir, S., Khan, M.Z., 2019a. Zinc oxide-decorated polypyrrole/chitosan bionanocomposites with enhanced photocatalytic, antibacterial and anticancer performance. RSC Adv. 9 (70), 41135–41150.

Ahmad, N., Sultana, S., Kumar, G., Zuhaib, M., Sabir, S., Khan, M.Z., 2019b. PANI based hybrid bionanocomposites with enhanced visible light photocatalytic activity and antifungal activity. J. Environ. Chem. Eng. 7 (1), 102804.

Alam, U., Khan, A., Ali, D., Bahnemann, D., Muneer, M., 2018. Comparative photocatalytic activity of sol–gel derived rare earth metal (La, Nd, Sm and Dy)-doped ZnO photocatalysts for degradation of dyes. RSC Adv. 8 (31), 17582–17594.

Almutairi, A., Weatherley, L.R., 2015. Intensification of ammonia removal from wastewater in biologically active zeolitic ion exchange columns. J. Environ. Manag. 160, 128–138.

Altomare, M., Chiarello, G.L., Costa, A., Guarino, M., Selli, E., 2012. Photocatalytic abatement of ammonia in nitrogen-containing effluents. Chem. Eng. J. 191, 394–401.

Arai, T., Yanagida, M., Konishi, Y., Iwasaki, Y., Sugihara, H., Sayama, K., 2007. Efficient complete oxidation of acetaldehyde into CO2 over $CuBi_2O_4/WO_3$ composite photocatalyst under visible and UV light irradiation. J. Phys. Chem. C 111 (21), 7574–7577.

Bahmani, M., Dashtian, K., Mowla, D., Esmaeilzadeh, F., Ghaedi, M., 2020. UiO-66 (Ti)-Fe_3O_4-WO_3 photocatalyst for efficient ammonia degradation from wastewater into continuous flow-loop thin film slurry flat-plate photoreactor. J. Hazard Mater. 393, 122360.

Bano, S., Ahmad, N., Sultana, S., Sabir, S., Khan, M.Z., 2019. Preparation and study of ternary polypyrrole-tin oxide-chitin nanocomposites and their potential applications in visible light photocatalysis and sensors. J. Environ. Chem. Eng. 7 (2), 103012.

Bano, D., Kumar, V., Singh, V.K., Chandra, S., Singh, D.K., Yadav, P.K., et al., 2018. A facile and simple strategy for the synthesis of label free carbon quantum dots from the latex of Euphorbia milii and its peroxidase-mimic activity for the naked eye detection of glutathione in a human blood serum. ACS Sustain. Chem. Eng. 7 (2), 1923–1932.

Bao, Y., Du, H., Chai, W.S., Nie, D., Zhou, L., 2022. Numerical investigation and optimization on laminar burning velocity of ammonia-based fuels based on GRI3. 0 mechanism. Fuel 318, 123681.

Belabed, C., Tab, A., Moulai, F., Černohorský, O., Boudiaf, S., Benrekaa, N., et al., 2021. ZnO nanorods-PANI heterojunction dielectric, electrochemical properties, and photodegradation study of organic pollutant under solar light. Int. J. Hydrogen Energy 46 (40), 20893–20904.

Chai, W.S., Bao, Y., Jin, P., Tang, G., Zhou, L., 2021a. A review on ammonia, ammonia-hydrogen and ammonia-methane fuels. Renew. Sustain. Energy Rev. 147, 111254.

Chai, W.S., Chew, C.H., Munawaroh, H.S.H., Ashokkumar, V., Cheng, C.K., Park, Y.K., Show, P.L., 2021b. Microalgae and ammonia: a review on inter-relationship. Fuel 303, 121303.

Dubois, I.E., Holgersson, S., Allard, S., Malmström, M.E., 2011. Dependency of BET surface area on particle size for some granitic minerals. Proc. Radiochem. 1 (1), 75–82.

Goransson, D.J.O., Borgstrom, M.T., Huang, Y.Q., Messing, M.E., Hessman, D., Buyanova, I.A., et al., 2019. Measurements of strain and bandgap of coherently epitaxially grown wurtzite InAsP–InP core–shell nanowires. Nano Lett. 19 (4), 2674–2681.

Guo, F., Shi, W., Wang, H., Huang, H., Liu, Y., Kang, Z., 2017. Fabrication of a $CuBi_2O_4$/g-C_3N_4 p–n heterojunction with enhanced visible light photocatalytic efficiency toward tetracycline degradation. Inorg. Chem. Front. 4 (10), 1714–1720.

He, S., Hou, P., Petropoulos, E., Feng, Y., Yu, Y., Xue, L., Yang, L., 2018. High efficient visible-light photocatalytic performance of Cu/ZnO/rGO nanocomposite for decomposing of aqueous ammonia and treatment of domestic wastewater. Front. Chem. 6, 219.

Kundu, S., Satpati, B., Kar, T., Pradhan, S.K., 2017. Microstructure characterization of hydrothermally synthesized PANI/V_2O_5· nH_2O heterojunction photocatalyst for visible light induced photodegradation of organic pollutants and non-absorbing colorless molecules. J. Hazard Mater. 339, 161–173.

Li, J., Xu, K., Liu, T., Bai, G., Liu, Y., Wang, C., Zheng, M., 2019. Achieving stable partial nitritation in an acidic nitrifying bioreactor. Environ. Sci. Technol. 54 (1), 456–463.

Liu, S.Q., Zhu, X.L., Zhou, Y., Meng, Z.D., Chen, Z.G., Liu, C.B., et al., 2017. Smart photocatalytic removal of ammonia through molecular recognition of zinc ferrite/reduced graphene oxide hybrid catalyst under visible-light irradiation. Catal. Sci. Technol. 7 (15), 3210–3219.

Liu, W.X., Zhu, X.L., Liu, S.Q., Gu, Q.Q., Meng, Z.D., 2018. Near-infrared-driven selective photocatalytic removal of ammonia based on valence band recognition of an α-MnO_2/N-doped graphene hybrid catalyst. ACS Omega 3 (5), 5537–5546.

Mitra, M., Ahamed, S.T., Ghosh, A., Mondal, A., Kargupta, K., Ganguly, S., Banerjee, D., 2019. PANI/reduced graphene oxide composite-enhanced visible-light-driven photocatalytic activity for the degradation of organic dyes. ACS Omega 4 (1), 1623–1635.

Mohammadi, Z., Sharifnia, S., Shavisi, Y., 2016. Photocatalytic degradation of aqueous ammonia by using TiO_2 ZnO/LECA hybrid photocatalyst. Mater. Chem. Phys. 184, 110–117.

Peng, X., Wang, M., Hu, F., Qiu, F., Dai, H., Cao, Z., 2019. Facile fabrication of hollow biochar carbon-doped TiO_2/CuO composites for the photocatalytic degradation of ammonia nitrogen from aqueous solution. J. Alloys Compd. 770, 1055–1063.

Pressley, T.A., Bishop, D.F., Roan, S.G., 1972. Ammonia-nitrogen removal by breakpoint chlorination. Environ. Sci. Technol. 6 (7), 622–628.

Qiang, J., Zhou, Z., Wang, K., Qiu, Z., Zhi, H., Yuan, Y., et al., 2020. Coupling ammonia nitrogen adsorption and regeneration unit with a high-load anoxic/aerobic process to achieve rapid and efficient pollutants removal for wastewater treatment. Water Res. 170, 115280.

Ren, G., Han, H., Wang, Y., Liu, S., Zhao, J., Meng, X., Li, Z., 2021. Recent advances of photocatalytic application in water treatment: a review. Nanomaterials 11 (7), 1804.

Sethuraman, S., Marimuthu, A., Kattamuthu, R., Karuppasamy, G., 2021. Highly surface active niobium doped g-C_3N_4/g-C_3N_4 heterojunction interface towards superior photocatalytic and selective ammonia response. Appl. Surf. Sci. 561, 150077.

Shafi, A., Ahmad, N., Sultana, S., Sabir, S., Khan, M.Z., 2019. Ag_2S-sensitized NiO–ZnO heterostructures with enhanced visible light photocatalytic activity and acetone sensing property. ACS Omega 4 (7), 12905–12918.

Sharma, G., Zhao, Z., Sarker, P., Nail, B.A., Wang, J., Huda, M.N., Osterloh, F.E., 2016. Electronic structure, photovoltage, and photocatalytic hydrogen evolution with p-$CuBi_2O_4$ nanocrystals. J. Mater. Chem. 4 (8), 2936–2942.

Shavisi, Y., Sharifnia, S., 2018. Deriving Ag_3PO_4 single bond CaO composite as a stable and solar light photocatalyst for efficient ammonia degradation from wastewater. J. Energy Chem. 27 (1), 290–299.

Shavisi, Y., Sharifnia, S., Hosseini, S.N., Khadivi, M.A., 2014a. Application of TiO_2/perlite photocatalysis for degradation of ammonia in wastewater. J. Ind. Eng. Chem. 20 (1), 278–283.

Shavisi, Y., Sharifnia, S., Zendehzaban, M., Mirghavami, M.L., Kakehazar, S., 2014b. Application of solar light for degradation of ammonia in petrochemical wastewater by a floating TiO_2/LECA photocatalyst. J. Ind. Eng. Chem. 20 (5), 2806–2813.

Shi, W., Guo, F., Yuan, S., 2017. In situ synthesis of Z-scheme $Ag_3PO_4/CuBi_2O_4$ photocatalysts and enhanced photocatalytic performance for the degradation of tetracycline under visible light irradiation. Appl. Catal. B Environ. 209, 720–728.

Tang, G., Jin, P., Bao, Y., Chai, W.S., Zhou, L., 2021. Experimental investigation of premixed combustion limits of hydrogen and methane additives in ammonia. Int. J. Hydrogen Energy 46 (39), 20765–20776.

Tanwar, R., Kaur, B., Mandal, U.K., 2017. Highly efficient and visible light driven Ni0. 5Zn0. $5Fe_2O_4$@ PANI modified BiOCl heterocomposite catalyst for water remediation. Appl. Catal. B Environ. 211, 305–322.

Tian, Y., Li, W., Zhao, C., Wang, Y., Zhang, B., Zhang, Q., 2017. Fabrication of hollow mesoporous SiO_2-BiOCl@ PANI@ Pd photocatalysts to improve the photocatalytic performance under visible light. Appl. Catal. B Environ. 213, 136–146.

Ukwuani, A.T., Tao, W., 2016. Developing a vacuum thermal stripping–acid absorption process for ammonia recovery from anaerobic digester effluent. Water Res. 106, 108–115.

Wang, M., Zai, J., Wei, X., Chen, W., Liang, N., Xu, M., et al., 2015. N-type hedgehog-like $CuBi_2O_4$ hierarchical microspheres: room temperature synthesis and their photoelectrochemical properties. CrystEngComm 17 (21), 4019–4025.

Wang, Y., Li, F., Xue, T., Liu, C., Yuan, D., Qi, F., Xu, B., 2018. Heterogeneous activation of peroxymonosulfate by hierarchical $CuBi_2O_4$ to generate reactive oxygen species for refractory organic compounds degradation: morphology and surface chemistry derived reaction and its mechanism. Environ. Sci. Pollut. Control Ser. 25 (5), 4419–4434.

Xiong, J., Zeng, H.Y., Chen, C.R., Peng, D.Y., Xu, S., An, D.S., 2022. Conjugated hollow polyaniline/$CuBi_2O_4$ composite with enhanced photocatalytic activity under visible-light. Surface. Interfac. 29, 101804.

Xu, X., Liu, R., Cui, Y., Liang, X., Lei, C., Meng, S., et al., 2017. PANI/FeUiO-66 nanohybrids with enhanced visible-light promoted photocatalytic activity for the selectively aerobic oxidation of aromatic alcohols. Appl. Catal. B Environ. 210, 484–494.

Yan, S., Song, H., Li, Y., Yang, J., Jia, X., Wang, S., Yang, X., 2022. Integrated reduced graphene oxide/polypyrrole hybrid aerogels for simultaneous photocatalytic decontamination and water evaporation. Appl. Catal. B Environ. 301, 120820.

Ye, J., Liu, S.Q., Liu, W.X., Meng, Z.D., Luo, L., Chen, F., Zhou, J., 2019. Photocatalytic simultaneous removal of nitrite and ammonia via a zinc ferrite/activated carbon hybrid catalyst under UV–visible irradiation. ACS Omega 4 (4), 6411–6420.

Zhang, G., Ruan, J., Du, T., 2020. Recent advances on photocatalytic and electrochemical oxidation for ammonia treatment from water/wastewater. ACS ES&T Engineering 1 (3), 310–325.

Zheng, L., Sun, X., Zhang, R., Gao, J., Feng, D., He, J., et al., 2021. Enhanced photocatalytic performance of ammonia self-etched holely g-C_3N_4 decorated with anatase nanoflakes by a facile synthesis process. Appl. Surf. Sci. 542, 148580.



https://dspace.org/

A novel CuBi2O4/polyaniline composite as an efficient photocatalyst for ammonia degradation

Ahmad, Nafees; Anae, Jerry; Khan, Mohammad Zain; Sabir, Suhail; Campo Moreno, Pablo ...

2022-08-17
Elsevier
https://doi.org/10.1016/j.heliyon.2022.e10210
Ahmad N, Anae J, Khan MZ, et al., (2022) A novel CuBi2O4/polyaniline composite as an efficient photocatalyst for ammonia degradation, Heliyon, Volume 8, Issue 8, August 2022, Article number e10210

Downloaded from a DSpace repository. https://dspace.org/